Sequential Cesium Incorporation for Highly Efficient Formamidinium-Cesium Perovskite Solar Cells

Haoran Chen[1†], Yong Wang[2†], Yingping Fan[1†], Yuetian Chen[1], Yanfeng Miao[1], Zhixiao Qin[1], Xingtao Wang[1], Xiaomin Liu[1], Kaicheng Zhu[1], Feng Gao[2]*, Yixin Zhao[1,3]*

Affiliations:

[1]School of Environmental Science and Engineering, Frontiers Science Center for Transformative Molecules, Shanghai Jiao Tong University, Shanghai 200240, China.

[2] Department of Physics, Chemistry and Biology (IFM), Linköping University, 581 83 Linköping, Sweden.

[3] Shanghai Institute of Pollution Control and Ecological Security, Shanghai 200240, China.

† These authors contributed equally to this work

*Corresponding author. Email: yixin.zhao@sjtu.edu.cn, feng.gao@liu.se

Abstract: Although pure formamidinium iodide perovskite ($FAPbI_3$) possesses an optimal gap for photovoltaics, their poor phase stability limits the long-term operational stability of the devices. A promising approach to enhance their phase stability is to incorporate cesium into $FAPbI_3$. However, state-of-the-art formamidinium-cesium (FA-Cs) iodide perovskites demonstrate much worse efficiency compared with $FAPbI_3$, limited by different crystallization dynamics of formamidinium and cesium, which result in poor composition homogeneity and high trap densities. We develop a novel strategy of crystallization decoupling processes of formamidinium and cesium via a sequential cesium incorporation approach. As such, we obtain highly reproducible and highly efficient solar cells based on $FA_{1-x}Cs_xPbI_3$ films, with uniform composition distribution and low defect densities. In addition, our cesium-incorporated perovskites demonstrate much enhanced stability compared with $FAPbI_3$, as a result of suppressed ionic migration due to reduced electron-phonon coupling.

Metal-halide perovskites with superior photophysical properties and low-cost solution process have emerged as promising candidates for different optoelectronic devices, including solar cells, light-emitting diodes, *etc(1-3)*. For perovskite solar cells (PSCs), different compositions have been attempted for high efficiencies. Among others, formamidinium lead iodide ($FAPbI_3$) have promised great potential, due to their optimal band-gap of ~1.5 eV and excellent thermal stability(*4-6*).

However, the photoactive $FAPbI_3$ black phase would easily transform into a non-photoactive yellow δ-$FAPbI_3$ phase at room temperature, especially under humid conditions. The poor phase stability challenges both efficiency and long-term stability of PSCs based on $FAPbI_3$(*7, 8*). It is generally believed that the phase instability of $FAPbI_3$ perovskites originates from its unsuitable tolerant factor. To address this problem, alloying FA^+ with MA^+/Cs^+ cations or partially substituting I^- with Br^- ions have been employed to tune the tolerant factor(*9-11*). The resulting mixed-ion FA-based perovskites exhibit improved resistance to phase transition.

Among these different alloying approaches, formamidinium-cesium mixed-cation pure iodide ($FA_{1-x}Cs_xPbI_3$) perovskites are particularly promising, because they avoid the concerns on volatile MA cations and phase segregation induced by mixed halide ions (Br-I)(*12-15*). However, because of the complex crystallization dynamics of formamidinium and cesium, these pure iodide FA-Cs perovskites suffer from poor composition homogeneity and high defects/traps densities(*16, 17*). The PSCs based on these films are therefore facing relatively low efficiencies. Especially, strong non-radiative recombination in all reported FA-Cs based PSCs limited the open-circuit voltage (V_{oc}) of the resulting devices(*18, 19*).

Herein, we decouple the crystallization processes of formamidinium and cesium through a sequential Cs incorporation strategy, and achieve highly efficient $FA_{1-x}Cs_xPbI_3$ (x=0.05-0.16) perovskites. The ratio of FA and Cs in $FA_{1-x}Cs_xPbI_3$ can be straightforwardly tuned by

introducing different content of Cs on the FA-based perovskite precursor film during the sequential Cs incorporation process. The resulting $FA_{1-x}Cs_xPbI_3$ perovskites show enhanced phase stability and reduced defects/trap density. As a result, the champion $FA_{0.91}Cs_{0.09}PbI_3$ PSCs yield a record power conversion efficiency (PCE) of 24.7% (certified stabilized 23.8%) with improved V_{oc} and fill factor (*FF*), which is the highest efficiency for the pure iodide $FA_{1-x}Cs_xPbI_3$ perovskites. Compared with $FAPbI_3$, the $FA_{0.91}Cs_{0.09}PbI_3$ perovskite shows reduced electron-phonon coupling and lattice fluctuations, contributing to the excellent operational stability of the $FA_{0.91}Cs_{0.09}PbI_3$ based PSCs.

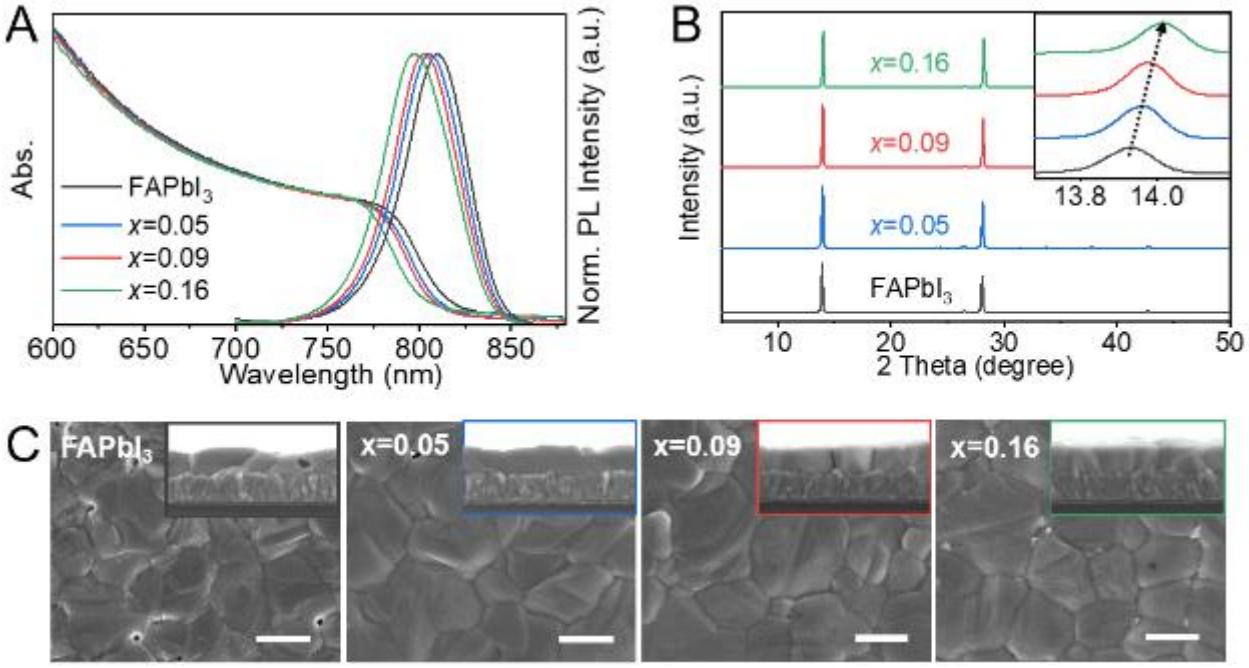

Fig. 1. (A) UV-vis absorption and normalized PL spectra and (B) XRD patterns of $FAPbI_3$ and $FA_{1-x}Cs_xPbI_3$ perovskites, inset pattern corresponding to (110) perovskite characteristic peaks. (C) Top-surface images of $FAPbI_3$ and $FA_{1-x}Cs_xPbI_3$ perovskite films. The inset presents the cross-sectional morphology of the corresponding perovskite films. The scale bars are 1 μm.

The $FA_{1-x}Cs_xPbI_3$ perovskite films are firstly prepared by the crystallization decoupling engineering. A $FAPbI_3$ precursor film is firstly deposited by a typical anti-solvent method. The Cs is sequentially introduced onto the FA perovskite film. For comparison, we employed different content of Cs to fabricate $FA_{1-x}Cs_xPbI_3$ perovskites. The final ratios of Cs in the $FA_{1-x}Cs_xPbI_3$ perovskite films, i.e., the value of *x*, are 0.05, 0.09 and 0.16, as confirmed by inductively coupled plasma-mass spectrometry (ICP-MS) analysis (Table S1). The corresponding $FA_{1-x}Cs_xPbI_3$ perovskite films are noted as x=0.05, x=0.09, x=0.16.

Optical and structural measurements of perovskite films indicate that Cs has successfully been incorporated into the lattice of $FAPbI_3$ perovskites. Fig. 1A shows the ultraviolet-visible (UV-vis) spectra of $FA_{1-x}Cs_xPbI_3$ perovskite films, in which the absorption edges of $FA_{1-x}Cs_xPbI_3$ perovskites strongly depend on the amount of Cs incorporation. When x increases from 0 to 0.16, the absorption edge of $FA_{1-x}Cs_xPbI_3$ perovskites gradually blue-shifts from 816 nm to 802 nm, and the corresponding photoluminescence (PL) peaks shift from 809 nm to 797 nm. The X-ray diffraction (XRD) measurements are carried out to investigate the crystal structure evolution of $FA_{1-x}Cs_xPbI_3$ perovskites (Fig. 1B). All the $FA_{1-x}Cs_xPbI_3$ perovskites exhibit stronger peak intensity than the pure $FAPbI_3$ film, suggesting that sequential Cs incorporation enhances the overall crystallinity of perovskite films. The inset image of Fig. 1B shows that the (110) peak between 13.8°-14.1° shifts to a higher degree, indicating that Cs are incorporated into the perovskite lattice. The tolerance factor of $FA_{1-x}Cs_xPbI_3$ perovskites also reduced compared with pure FA perovskite, which expected to stabilize perovskite structure (fig. S1).

The Cs incorporation also significantly improves the film morphologies (Fig. 1C). All $FA_{1-x}Cs_xPbI_3$ films show enlarged and pinhole-free grains compared to the $FAPbI_3$ film, which shows coarse grains and pinholes. As shown in the cross-sectional images, $FA_{1-x}Cs_xPbI_3$ perovskite

films (550 to 600 nm) are composed of micrometer-sized grains comparable to the film thickness, benefiting efficient charge extraction.

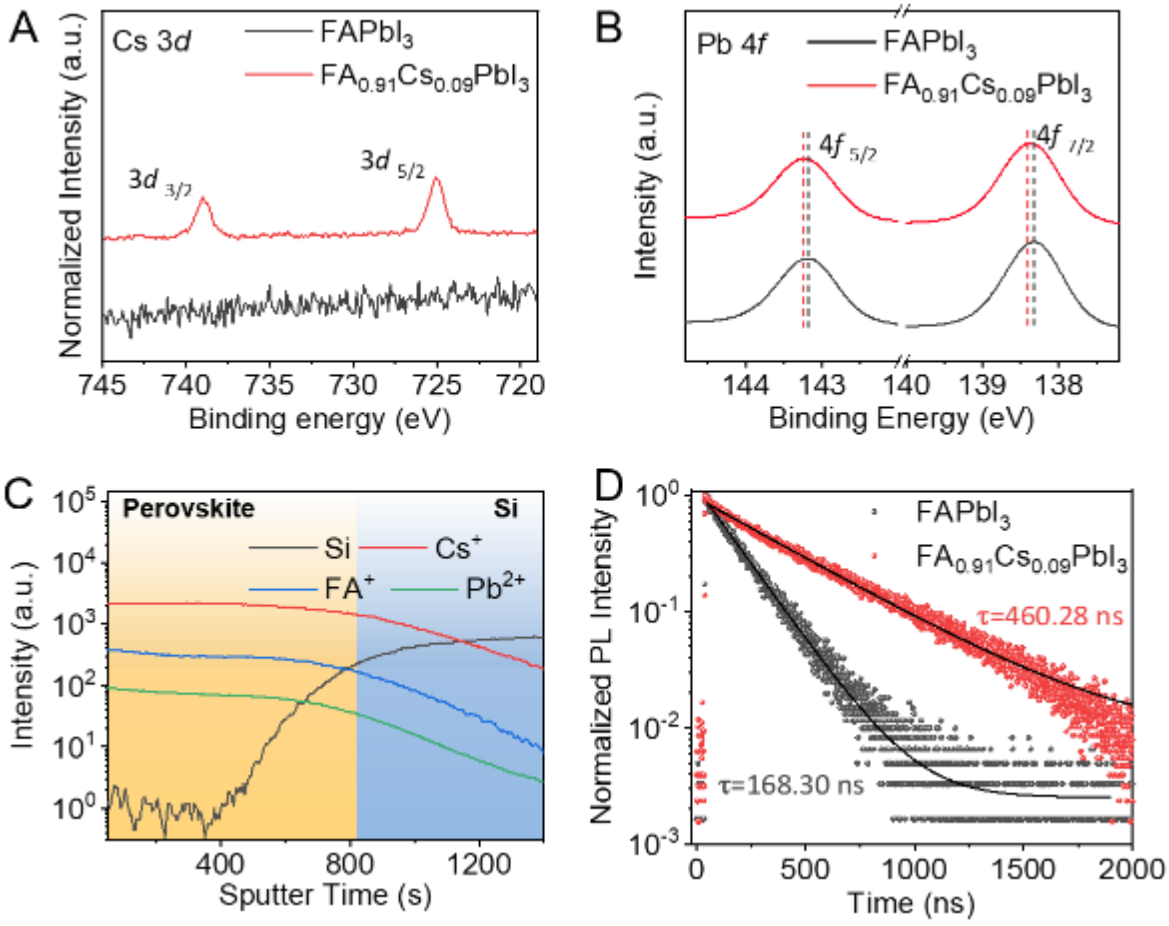

Fig. 2. XPS spectra of (A) Cs 3*d* and (B) Pb 4*f* in $FA_{0.91}Cs_{0.09}PbI_3$ and $FAPbI_3$ films. (C) ToF-SIMS depth profiling analysis in the $FA_{0.91}Cs_{0.09}PbI_3$ film. (D) TRPL decay curves of $FAPbI_3$ and $FA_{0.91}Cs_{0.09}PbI_3$ perovskite films.

By adopting these Cs-incorporated perovskites as light absorber layers, we fabricate PSCs with a configuration of FTO/electron-transport layer/perovskite/hole-transport layer/Au. All $FA_{1-x}Cs_xPbI_3$ (x=0.05, 0.09, 0.16) based PSCs exhibit improved device efficiency compared with the $FAPbI_3$ based device (fig. S2). Considering that x=0.09 provides the optimal photovoltaic (PV) performance, we then chose the case of $FA_{0.91}Cs_{0.09}PbI_3$ for detailed investigations on Cs incorporation and its role on film and device properties.

X-ray photoelectron spectroscopy (XPS) spectra are conducted to explore the effect of sequential Cs incorporation on the chemical composition of perovskite films. All core-level peaks are assigned to Cs, Pb, I, C, and N (Fig. 2A, 2B, and fig. S3). Fig. 2A shows that the characteristic Cs signals in the $FA_{0.91}Cs_{0.09}PbI_3$ perovskite locate at 738.5 eV and 724.7 eV. For the Pb 4*f* spectra in $FAPbI_3$, two peaks corresponding to Pb $4f_{7/2}$ and Pb $4f_{5/2}$ are observed at 138.3 eV and 143.2eV. However, in the case of $FA_{0.91}Cs_{0.09}PbI_3$ perovskite, both Pb $4f_{7/2}$ and Pb $4f_{5/2}$ shift 0.1 eV toward higher binding energy, originating from stronger bond energies between Cs^+ and $[PbI_6]^{4-}$ than that between FA^+ and $[PbI_6]^{4-}$. Additionally, the N and I elements representing the formamidine component have undergone a small shift (fig. S3). These results further confirm that Cs has been successfully incorporated into the $FAPbI_3$ perovskite lattice to form $FA_{0.91}Cs_{0.09}PbI_3$ perovskite.

Since the distribution of Cs in $FA_{1-x}Cs_xPbI_3$ perovskite has a significant effect on both the phase stability and traps/defects(*11, 20*), we proceed to investigate the distribution of Cs in the resulting $FA_{0.91}Cs_{0.09}PbI_3$ perovskite. The energy dispersive spectroscopy (EDS) mapping and time-of-flight secondary ion mass spectrometry (ToF-SIMS) establish that the incorporated Cs homogenously distributes in the surface and bulk of $FA_{0.91}Cs_{0.09}PbI_3$ perovskite (Fig. 2C and fig. S4). In addition, other ions, including FA^+, Pb^{2+} and I^-, are also uniformly distributed throughout the $FA_{0.91}Cs_{0.01}PbI_3$ perovskite film (fig. S5). Such uniform distribution of Cs ions is beneficial to improve the phase stability and reduce defect concentration. (Fig. 2C).

Uniform incorporation of Cs ions into $FAPbI_3$ has two positive effects: enhanced phase stability of the photoactive black phase and decreased trap/defect densities. The enhanced phase stability is evidenced from the absence of color/structural changes under humid conditions. Under 60% relative humidity, $FA_{0.91}Cs_{0.09}PbI_3$ maintains the black phase for 7 days without any changes (fig.

S6), showing significant improvement compared with $FAPbI_3$. The decreased trap/defect densities are demonstrated from photophysical measurements. The photoluminescence (PL) intensities of $FA_{0.91}Cs_{0.09}PbI_3$ perovskites are much stronger than those of pure FA perovskite films (fig. S7). In addition, the time-resolved PL (TRPL) spectra in Fig. 2D show that the PL lifetime (τ) of $FA_{0.91}Cs_{0.09}PbI_3$ is much longer (413.84 ns) than that of $FAPbI_3$ (165.49 ns). Enhanced PL intensity and improved PL lifetime indicate that non-radiative recombination is suppressed in $FA_{0.91}Cs_{0.09}PbI_3$, attributed to decreased trap densities. Consistently, the Urbach energy (fig. S8) is decreased from 22.2 meV in $FAPbI_3$ to 18.3 meV in $FA_{0.91}Cs_{0.09}PbI_3$. The smaller Urbach energy in $FA_{0.91}Cs_{0.09}PbI_3$ corresponds to a lower density of trap states. These results suggest that, with incorporation of Cs, the $FA_{0.91}Cs_{0.09}PbI_3$ perovskite exhibits significantly reduced non-radiative recombination via defects/traps.

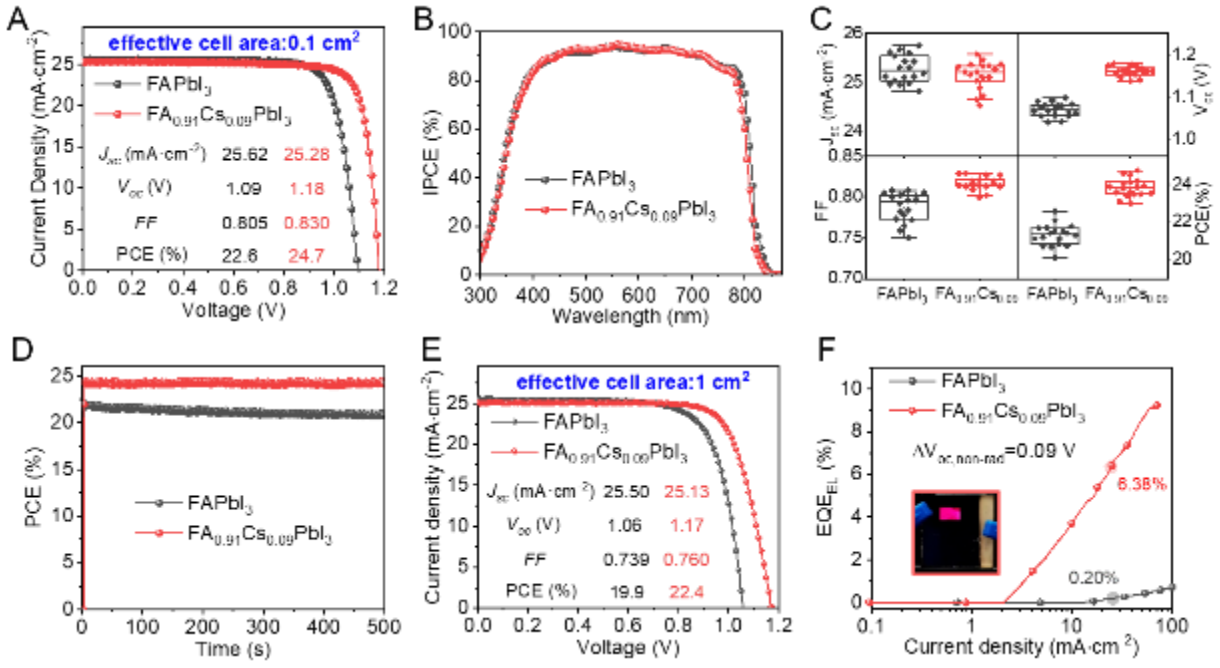

Fig. 3. (A) The J-V curves of the champion devices of $FAPbI_3$ and $FA_{0.91}Cs_{0.09}PbI_3$ PSCs with 0.1 cm^2 effective cell area. (B) IPCE spectra of $FAPbI_3$ and $FA_{0.91}Cs_{0.09}PbI_3$ based PSCs. (C) The PV performance distribution of $FAPbI_3$ and $FA_{0.91}Cs_{0.09}PbI_3$ based PSCs from 18 devices,

respectively. (D) Steady state efficiency of $FAPbI_3$ and $FA_{0.91}Cs_{0.09}PbI_3$ PSCs. (E) J-V characteristics of PSCs based on $FAPbI_3$ and $FA_{0.91}Cs_{0.09}PbI_3$ with 1 cm^2 effective cell area under simulated AM 1.5G solar illumination of 100 $mW \cdot cm^{-2}$ in reverse scan. (F) EQE_{EL} of $FAPbI_3$ and $FA_{0.91}Cs_{0.09}PbI_3$ based PSCs versus (vs.) the current density.

Benefiting from these advantages of crystallization decoupling engineering, the resulting $FA_{0.91}Cs_{0.09}PbI_3$ shows much enhanced device performance. Fig. 3A compares the current density-voltage (*J-V*) characteristics of champion PSCs based on $FAPbI_3$ and $FA_{0.91}Cs_{0.09}PbI_3$ perovskites, respectively. The $FA_{0.91}Cs_{0.09}PbI_3$-based PSC exhibits an impressive PCE of 24.7%, compared with 22.6% for $FAPbI_3$. We also obtained a certified PCE of 23.8% with neglected hysteresis for $FA_{0.91}Cs_{0.09}PbI_3$-based PSC (fig. S9). The most striking difference is the V_{oc}, which increases from 1.09 V in $FAPbI_3$ to 1.18V in $FA_{0.91}Cs_{0.09}PbI_3$. The incident photon to electron conversion efficiency (IPCE) (Fig. 3B) is similar for both devices, with a high value over 90% in the wavelength range of 450~650 nm. The short-circuit current density (J_{sc}) of the $FA_{0.91}Cs_{0.09}PbI_3$ device is slightly decreased compared with the $FAPbI_3$ device, mainly due to slight increase of the bandgap upon Cs incorporation. Fig. 3C compares the PV parameters of $FAPbI_3$- and $FA_{0.91}Cs_{0.09}PbI_3$- based PSCs for 18 devices respectively, indicating that Cs incorporation also improves the device reproducibility. In addition, the $FA_{0.91}Cs_{0.09}PbI_3$ based PSCs exhibit a smaller hysteresis (fig. S9 and S10), resulting in a stabilized output power of 24.4% (Fig. 3D), a new record for the pure iodide $FA_{1-x}Cs_xPbI_3$ based PSCs. We also fabricated large-area PSCs based on these Cs-incorporated perovskite films. The champion $FA_{0.91}Cs_{0.09}PbI_3$ device, fabricated on 2.5-cm by 2.5-cm substrates with an effective cell area of 1 cm^2 (Fig. 3E), display a PCE of 22.4%, which is far higher than that of $FAPbI_3$ devices (~19.9%).

The significantly enhanced V_{oc} of the $FA_{0.91}Cs_{0.09}PbI_3$ device is mainly due to suppressed non-radiative recombination, which can be quantified by measuring the external quantum efficiency of electroluminescence (EQE_{EL}) values (*21*). As shown in Fig. 3F, at the injection current densities corresponding to J_{sc}, the EQE_{EL} value of the $FA_{0.91}Cs_{0.09}PbI_3$ device is 6.38%, while that of the $FAPbI_3$ device is 0.16%. We calculate the voltage losses due to non-radiative recombination ($\Delta V_{oc,non\text{-}rad}$) based on the formula(*22*):

$$\Delta V_{\mathrm{oc,non-rad}} = \frac{\mathrm{k}T}{\mathrm{q}} \ln \mathrm{EQE_{EL}}$$

where k, T and q are Boltzmann constant, temperature, and elementary electric charge, respectively. The difference in $\Delta V_{\mathrm{oc,non\text{-}rad}}$ (0.09 V) matches well with the difference of device V_{oc} (0.09 V).

Suppressed non-radiative recombination in the $FA_{0.91}Cs_{0.09}PbI_3$ device is consistent with previous photophysical measurements on the films, which indicate that crystallization decoupling engineering can reduce the defects/traps in $FA_{0.91}Cs_{0.09}PbI_3$. Further measurements on the devices also reach similar conclusions. The trap-filled limiting voltage in the space-charge limited current (SCLC) measurements decreases from 0.13 V in the $FAPbI_3$ device to 0.09 V in $FA_{0.91}Cs_{0.09}PbI_3$ device (fig. S11), indicating suppressed traps/defects upon Cs sequential incorporation. These results are also consistent with transient photovoltage (TPV) decay and transient photocurrent (TPC) decay results (fig. S12), which show slower TPV decay (indicating longer recombination lifetime) and quicker TPC decay (indicating less trapping effects) in the $FA_{0.91}Cs_{0.09}PbI_3$ device.

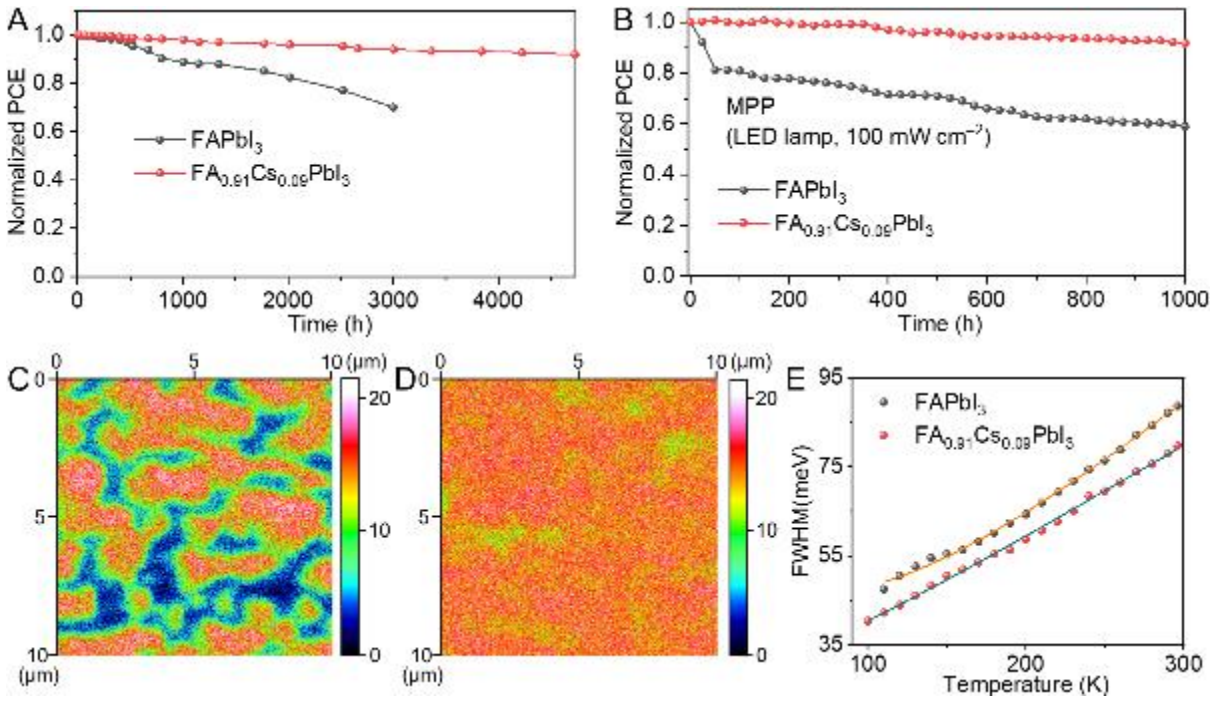

Fig. 4. (A) The shelf-life stability of the $FAPbI_3$ and $FA_{0.91}Cs_{0.09}PbI_3$ PSCs. (B) The long-term operational stability of $FAPbI_3$ and $FA_{0.91}Cs_{0.09}PbI_3$ PSCs. The I^- distribution in the middle of the perovskite layer (at ~300nm) for PSCs based on (C) $FAPbI_3$ and (D) $FA_{0.91}Cs_{0.09}PbI_3$ perovskites after 240 h operational stability test at MPP. (E) Fit of the FWHM of the PL spectra vs. temperature.

In addition to improved PV performance, the $FA_{0.91}Cs_{0.09}PbI_3$ device also shows significantly enhanced stability. We firstly measure the shelf life by storing the unencapsulated devices in dark at 25 °C and 20% relative humidity. Fig. 4A shows that the PCE of the $FAPbI_3$ device decreases by about 30% after 3,000 h aging, whereas the $FA_{0.91}Cs_{0.09}PbI_3$ device shows a degradation of only 10% over 4,500 h aging. We then investigate the long-term operational stability of the PSCs by aging the unencapsulated devices under a nitrogen atmosphere, using maximum power point (MPP) tracking under simulated 1-sun conditions. As shown in Figure 4B, the $FA_{0.91}Cs_{0.09}PbI_3$ based PSCs retains over 90% of the initial PCE while the $FAPbI_3$ device maintains only 60% PCE after 1000 h continuous illumination (fig. S13).

A main reason for enhanced stability PSCs is attributed to suppressed ionic migration. In Fig. 4C and 4D, we compare the I^- ions distribution at the ~300 nm depth of the perovskite layer for PSCs based on $FAPbI_3$ and $FA_{0.91}Cs_{0.09}PbI_3$ after 240 h MPP test. In the $FAPbI_3$-based device, strong aggregation of I^- clusters is observed in the perovskite absorber layers; in contrast, I^- ions distribute uniformly in the $FA_{0.91}Cs_{0.09}PbI_3$ based devices. This sharp contract indicates that, the ionic migration in the $FA_{0.91}Cs_{0.09}PbI_3$ is much suppressed upon Cs sequential incorporation.

Suppressed ionic migration in $FA_{0.91}Cs_{0.09}PbI_3$ is consistent with suppressed electron-phonon coupling upon Cs incorporation. Fig. 4E shows the full-width half-maximum (FWHM) of the PL peak of $FA_{0.91}Cs_{0.09}PbI_3$ and $FAPbI_3$ perovskites (fig. S14) ranging from 110 K to 296 K. The wide broadening of the PL linewidth in $FAPbI_3$ perovskites arises from strong electron-phonon coupling(*23*, *24*). The electron-phonon interaction is dominated by high energy LO phonons in the high-temperature region, where the measured FWHM data could be fitted by the Boson model (Fig. 4C, fig. S14, and Table S2). Compared with $FAPbI_3$, both electron-LO phonon coupling coefficient (Γ_{LO}) and LO phonon energy ($\hbar\omega$) in the $FA_{0.91}Cs_{0.09}PbI_3$ are significantly reduced, indicating that the fluctuation of the PbI_6 octahedra cage in $FA_{0.91}Cs_{0.09}PbI_3$ is associated with much smaller energies upon the Cs sequential incorporation. This is consistent with the previous theoretical investigations, which indicate that mixed A-site cations could reduce the lattice fluctuations in halide perovskites(*25*). As such, the suppressed lattice fluctuations and electron-phonon coupling in $FA_{0.91}Cs_{0.09}PbI_3$ rationalize suppressed ionic migration and hence enhanced stability in $FA_{0.91}Cs_{0.09}PbI_3$ PSCs.

In summary, we successfully develop a novel sequential Cs incorporation strategy to tackle the critical challenge on different crystallization dynamics of different cations in developing $FA_{1-x}Cs_xPbI_3$ perovskite PSCs. The resulting pure iodide $FA_{1-x}Cs_xPbI_3$ perovskites show uniform

composition distribution and reduced defects/traps density. Compared with $FAPbI_3$, the $FA_{0.91}Cs_{0.09}PbI_3$ exhibits reduced electron-phonon coupling and lattice fluctuations, minimizing ion migration and hence enhancing the stability. As such, we have been able to achieve highly stable PSCs with a high efficiency of 24.7%, a record for $FA_{1-x}Cs_xPbI_3$ PSCs. This work opens up new possibilities to develop high-quality mixed cation perovskites, presenting a milestone towards the development of highly efficient and highly stable perovskites for various applications, including solar cells, light-emitting diodes and lasers.

References

1. A. Kojima, K. Teshima, Y. Shirai, T. Miyasaka, Organometal Halide Perovskites as Visible-Light Sensitizers for Photovoltaic Cells. *J. Am. Chem. Soc.* **131**, 6050-6051 (2009).
2. H.-S. Kim *et al.*, Lead Iodide Perovskite Sensitized All-Solid-State Submicron Thin Film Mesoscopic Solar Cell with Efficiency Exceeding 9%. *Sci. Rep.* **2**, 591 (2012).
3. M. M. Lee, J. Teuscher, T. Miyasaka, T. N. Murakami, H. J. Snaith, Efficient Hybrid Solar Cells Based on Meso-Superstructured Organometal Halide Perovskites. *Science* **338**, 643 (2012).
4. G. E. Eperon *et al.*, Formamidinium lead trihalide: a broadly tunable perovskite for efficient planar heterojunction solar cells. *Energy Environ. Sci.* **7**, 982-988 (2014).
5. H. Lu *et al.*, Vapor-assisted deposition of highly efficient, stable black-phase $FAPbI_3$ perovskite solar cells. *Science* **370**, eabb8985 (2020).
6. W. Hui *et al.*, Stabilizing black-phase formamidinium perovskite formation at room temperature and high humidity. *Science* **371**, 1359 (2021).

7. Q. Han *et al.*, Single Crystal Formamidinium Lead Iodide ($FAPbI_3$): Insight into the Structural, Optical, and Electrical Properties. *Adv. Mater.* **28**, 2253-2258 (2016).
8. N. J. Jeon *et al.*, Compositional engineering of perovskite materials for high-performance solar cells. *Nature* **517**, 476-480 (2015).
9. W. Rehman *et al.*, Photovoltaic mixed-cation lead mixed-halide perovskites: links between crystallinity, photo-stability and electronic properties. *Energy Environ. Sci.* **10**, 361-369 (2017).
10. S.-H. Turren-Cruz, A. Hagfeldt, M. Saliba, Methylammonium-free, high-performance, and stable perovskite solar cells on a planar architecture. *Science* **362**, 449 (2018).
11. G. Kim *et al.*, Impact of strain relaxation on performance of α-formamidinium lead iodide perovskite solar cells. *Science* **370**, 108 (2020).
12. J.-W. Lee *et al.*, Formamidinium and Cesium Hybridization for Photo- and Moisture-Stable Perovskite Solar Cell. *Adv. Energy Mater.* **5**, 1501310 (2015).
13. Z. Li *et al.*, Stabilizing Perovskite Structures by Tuning Tolerance Factor: Formation of Formamidinium and Cesium Lead Iodide Solid-State Alloys. *Chem. Mater.* **28**, 284-292 (2016).
14. C. Yi *et al.*, Entropic stabilization of mixed A-cation ABX_3 metal halide perovskites for high performance perovskite solar cells. *Energy Environ. Sci.* **9**, 656-662 (2016).
15. Y. Deng *et al.*, Defect compensation in formamidinium-caesium perovskites for highly efficient solar mini-modules with improved photostability. *Nat. Energy*, (2021).
16. N. Li *et al.*, Microscopic Degradation in Formamidinium-Cesium Lead Iodide Perovskite Solar Cells under Operational Stressors. *Joule* **4**, 1743-1758 (2020).
17. H. Min *et al.*, Efficient, stable solar cells by using inherent bandgap of α-phase formamidinium lead iodide. *Science* **366**, 749 (2019).

18. J. Yang *et al.*, Crystallization tailoring of cesium/formamidinium double-cation perovskite for efficient and highly stable solar cells. *J. Energy Chem.* **48**, 217-225 (2020).

19. Z. Wang *et al.*, Efficient ambient-air-stable solar cells with 2D-3D heterostructured butylammonium-caesium-formamidinium lead halide perovskites. *Nat. Energy* **2**, 17135 (2017).

20. X. Zheng *et al.*, Improved Phase Stability of Formamidinium Lead Triiodide Perovskite by Strain Relaxation. *ACS Energy Lett.* **1**, 1014-1020 (2016).

21. Q. Jiang *et al.*, Surface passivation of perovskite film for efficient solar cells. *Nat. Photonics* **13**, 460-466 (2019).

22. W. Tress *et al.*, Predicting the Open-Circuit Voltage of $CH_3NH_3PbI_3$ Perovskite Solar Cells Using Electroluminescence and Photovoltaic Quantum Efficiency Spectra: the Role of Radiative and Non-Radiative Recombination. *Adv. Mater.* **5**, 1400812 (2015).

23. Z. Guo, X. Wu, T. Zhu, X. Zhu, L. Huang, Electron–Phonon Scattering in Atomically Thin 2D Perovskites. *ACS Nano* **10**, 9992-9998 (2016).

24. X. Gong *et al.*, Electron-phonon interaction in efficient perovskite blue emitters. *Nat. Mater.* **17**, 550-556 (2018).

25. D. Ghosh, P. Walsh Atkins, M. S. Islam, A. B. Walker, C. Eames, Good Vibrations: Locking of Octahedral Tilting in Mixed-Cation Iodide Perovskites for Solar Cells. *ACS Energy Lett.* **2**, 2424-2429 (2017).